ADVANCED FUNCTIONAL MATERIALS
www.afm-journal.de

Materials Views
www.MaterialsViews.com

Fabrication and Shell Optimization of Synergistic TiO_2-MoO_3 Core–Shell Nanowire Array Anode for High Energy and Power Density Lithium-Ion Batteries

*Chong Wang, Lingxia Wu, Hai Wang, Wenhua Zuo, Yuanyuan Li, and Jinping Liu**

A novel synergistic TiO_2-MoO_3 (TO-MO) core–shell nanowire array anode has been fabricated via a facile hydrothermal method followed by a subsequent controllable electrodeposition process. The nano-MoO_3 shell provides large specific capacity as well as good electrical conductivity for fast charge transfer, while the highly electrochemically stable TiO_2 nanowire core (negligible volume change during Li insertion/desertion) remedies the cycling instability of MoO_3 shell and its array further provides a 3D scaffold for large amount electrodeposition of MoO_3. In combination of the unique electrochemical attributes of nanostructure arrays, the optimized TO-MO hybrid anode (mass ratio: ca. 1:1) simultaneously exhibits high gravimetric capacity (ca. 670 mAh g^{-1}; approaching the hybrid's theoretical value), excellent cyclability (>200 cycles) and good rate capability (up to 2000 mA g^{-1}). The areal capacity is also as high as 3.986 mAh cm^{-2}, comparable to that of typical commercial LIBs. Furthermore, the hybrid anode was assembled for the first time with commercial $LiCoO_2$ cathode into a Li ion full cell, which shows outstanding performance with maximum power density of 1086 W kg_{total}^{-1} (based on the total mass of the TO-MO and $LiCoO_2$) and excellent energy density (285 Wh kg_{total}^{-1}) that is higher than many previously reported metal oxide anode-based Li full cells.

1. Introduction

Rechargeable lithium ion batteries (LIBs) with relatively high energy density and long-cycle stability are the most dominant power source for portable electronic devices in the present market.[1–7] However, as the rapid increase in global demand for much higher energy and power applications such as hybrid electric vehicles, flexible/wearable electronics and even micro-/nanoelectromechanical systems,[8–16] the current commercialized graphite anode with a relatively low theoretical capacity of 372 mAh g^{-1} and limited rate capability[17,18] cannot meet the requirements. Thus, to boost the electrochemical performance and application potential of the current LIB device, developing new anode materials simultaneously with relatively high capacity and high rate while maintaining good cycling stability is indispensable.

Transition metal oxides, which allow reversible insertion/deinsertion of Li^+ or react with Li^+ via a conversion process, have been considered as a promising anode candidate to address the challenge for high capacity.[19,20] With low electrical resistivity, high chemical stability and a superior theoretical capacity of around 1111 mAh g^{-1}[21] (ca. three times of graphite), MoO_3 has drawn particular interest as intriguing anode material used in LIBs.[22–24] But, the poor kinetics of Li ion diffusion in bulk MoO_3 and the drastic destruction of the structure caused by large volume expansion when forming Mo and Li_2O during the conversion reaction have hindered its practical application.[25,26] As demonstrated, after the initial high capacity of more than 600 mAh g^{-1}, the capacity of the 20th cycle decreased to less than 50% for micrometer-sized MoO_3, which also cannot be cycled at rates higher than 1 C.[27] Since nanomaterials in general exhibit peculiar and fascinating properties than the bulk counterparts, MoO_3 has been engineered into different nano-sized morphologies such as nanowires,[28,29] nanobelts,[30–35] micro/nanorods,[36] nanosheets,[37,38] and thin films[39,40] to improve the electrochemical properties. Benefiting from the large surface-to-volume ratio, short ion diffusion pathway and effective accommodation of induced stresses, electrodes from MoO_3 nanostructure powders have exhibited enhanced Li^+ storage. Despite much progress, the performance improvement by downsizing was very limited and ensuring facile electron transport in nanostructured MoO_3 electrodes is still highly desirable.

In recent years, many efforts have been gradually focused on the design of hybrid MoO_3-based electrodes to realize the

C. Wang, Prof. J. Liu
School of Chemistry
Chemical Engineering and Life Science and
State Key Laboratory of Advanced Technology for Materials Synthesis and Processing
Wuhan University of Technology
Wuhan, Hubei 430070, P. R. China
E-mail: liujp@whut.edu.cn
C. Wang, L. Wu, H. Wang, W. Zuo, Prof. J. Liu
Institute of Nanoscience and Nanotechnology
Department of Physics
Central China Normal University
Wuhan, Hubei 430079, P. R. China
Prof. Y. Li
School of Optical and Electronic Information
Huazhong University of Science and Technology
Wuhan 430074, P. R. China

DOI: 10.1002/adfm.201500634

above purpose. To combine the different physical and electrochemical properties of different components and utilize the respective advantage to remedy the defect of others is a feasible way to enhance the electrochemical performance of metal oxides.[41–51] So far, the most popular hybrid MoO_3 electrode for LIBs is nano-MoO_3 composited with various kinds of nanocarbons.[52–55] In such cases, the graphitic carbon not only serves as highly conductive framework to facilitate the electron transport at the nano-/microscale, but also may help to buffer the volume expansion of nano-MoO_3 during the charging/discharging process. As a consequence, the rate and cycling performance has been much improved. For instance, Sun et al.[54] reported a molybdenum oxide/graphene nanoarchitecture that showed a cycling stability up to 70 cycles and good rate capability (ca. 67% capacity retention with increasing the current density from 1000 to 2000 mA g^{-1}). Nevertheless, the overall performance of the nanocarbon-MoO_3 hybrid electrodes largely relied on the fabrication process of nanocarbons (which directly determines the surface chemistry and graphitization degree, etc.) and the distribution homogeneity of nanocarbon within the electrode film. Rational synthesis of alternative MoO_3-based hybrid electrodes that simultaneously exhibit high capacity, good rate performance and much longer cycling lifetime (>200 times) remains a huge challenge, especially when conductive carbon is absent in the electrode. On the other hand, although the nano-MoO_3-based Li half cells have been widely studied, Li full cells assembled by pairing nano-MoO_3 anode with high-potential cathode have rarely been reported. The development of Li full cells from nano-MoO_3 with high energy and power densities as well as stable cycleability would be of great significance to unveil the practical application potentials of MoO_3-based LIB anodes.

Herein, we report the fabrication of a new kind of MoO_3-based hybrid LIB anode, that is, synergistic TiO_2-MoO_3 (TO-MO) core–shell nanowire array via a facile hydrothermal growth of ordered TiO_2 nanowire followed by a subsequent controllable electrodeposition of nano-MoO_3; we further demonstrate the construction of high energy and power density $LiCoO_2$/TO-MO (LCO/TO-MO) full cell. As illustrated in **Figure 1**, strong synergistic effect exists in our anode design: (1) nano-TiO_2, as a nearly "zero strain" metal oxide anode (only ca. 4% volume change after lithiation), shows excellent cycle stability even at relatively high rates;[56–58] it is employed as an ideal partner (core) for optimizing MoO_3's cycleablity and rate performance. (2) The electrodeposited nano-MoO_3 shell, benefiting from the nanosize effect and its intrinsic characteristics, will provide both reversible large capacity and good electrical conductivity. (3) The specific architectural feature of binder-free single-crystalline TiO_2 nanowire array will simplify the electrode fabrication process, provide direct electron transport pathway between active material and current collector,[4,10a,b,11b,c,42] and facilitate the 3D uniform deposition of nano-MoO_3 with large areal mass loading, etc. After the optimization of the deposition amount of nano-MoO_3 shell, the synergistic TO-MO hybrid electrode (mass ratio is ca. 1:1) exhibits a high initial gravimetric capacity of ca. 670 mAh g^{-1} at the current density of 250 mA g^{-1}, long cycling up to 200 times and good rate performance. Furthermore, the areal capacity has been increased more than 10 times as compared to the pristine nano-MoO_3 film electrode which was electrodeposited without using TiO_2 nanowire array scaffold but under otherwise the same conditions. The initial areal capacity is as high as 3.986 mAh cm^{-2}, comparable to the level of typical commercial LIBs (3.7 mAh cm^{-2});[59,60] the areal capacity after 200 times cycling is still approaching or much superior to many previous values of thin film and 3D batteries,[61–68] including Si film-based LIB.

Using our TO-MO core–shell nanowire array as the anode and commercially available LCO film as the cathode, we further assembled a full-cell LIB, which shows a voltage plateau at ca. 3.3 V, a maximum energy density as high as 285 Wh kg_{total}^{-1} based on the total mass of TO-MO and LCO, a high power density (1086 W kg_{total}^{-1} at 114 Wh kg_{total}^{-1}), and a long cycling performance (>100 cycles). Our work opens up an opportunity in the development of binder-free MoO_3-based hybrid anode for high-performance LIB full cells. The concept presented herein can be readily extended to other high-capacity electrode materials that are however inferior in terms of cycling and rate performance.

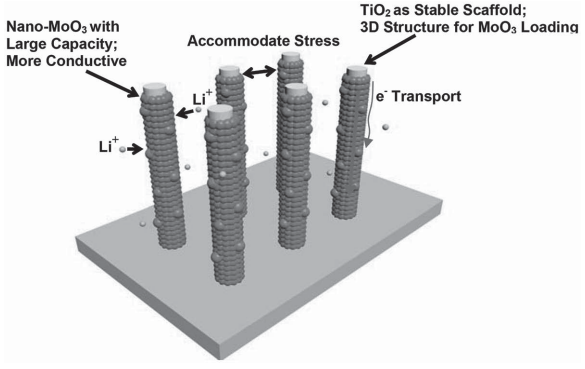

Figure 1. Schematic illustration of structural features of the synergistic TO-MO nanowire array.

2. Results and Discussion

2.1. Morphology and Structure of the Synergistic TO-MO Nanowire Array

Scanning electron microscopy (SEM) images of the pristine TiO_2 nanowire array and optimized TO-MO hybrid array anode on carbon cloth are shown in **Figure 2**a–d. We chose commercial carbon cloth as the current collector due to its high conductivity, lightweight, high chemical stability, and robust flexibility that makes it even applicable for flexible energy storage devices. As displayed in Figure 2a and its inset, after the hydrothermal growth, the whole surface of each carbon fiber is uniformly covered by numerous ordered TiO_2 nanowires with diameters of 50–100 nm and lengths of several mircometers. With the high aspect ratio of TiO_2 nanowires, the 3D nanoarray structure will provide enough spare space for loading plentiful MoO_3 shell materials and for sufficient contact with the electrolyte. The inserted image in Figure 2b shows the optical image of the optimized TO-MO hybrid electrode. It can be observed that the entire surface of the carbon cloth was covered homogeneously with a gray film after further electrodeposition. Figure 2b–d illustrates the typical SEM images of the TO-MO electrode

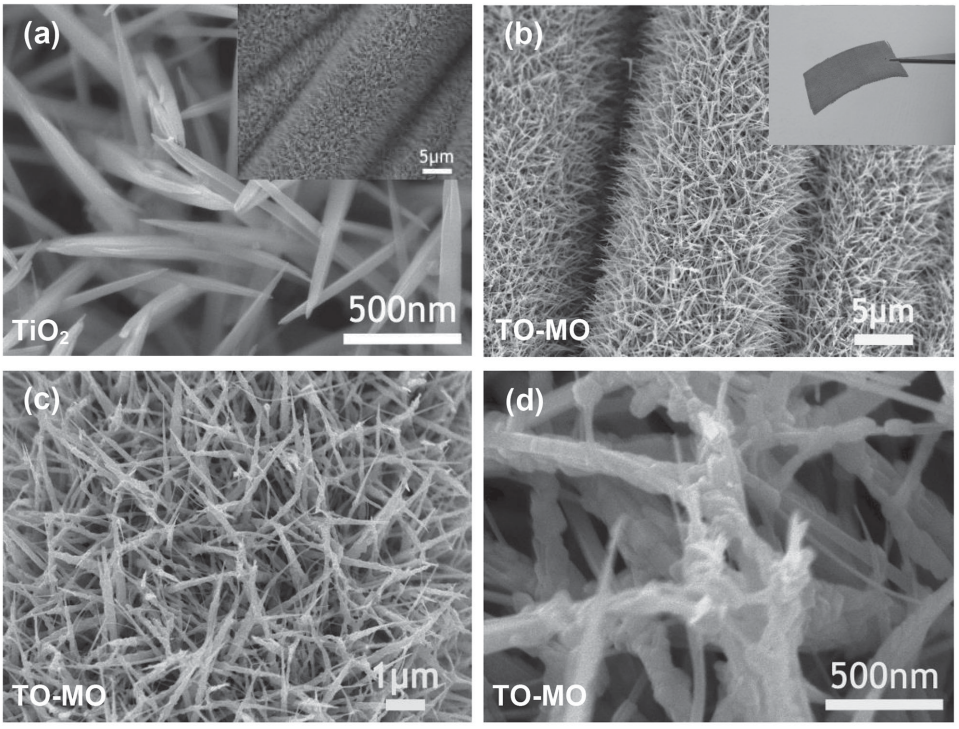

Figure 2. a) SEM images of the pristine TiO_2 nanowire array (inset: the low-resolution image). b–d) SEM images of the optimized TO-MO hybrid array anode with different magnifications (inset in Figure 2b is the optical image).

at different resolutions. After the deposition of MoO_3 materials, the resulting TO-MO nanowires still strongly adhere to the underlying substrate. They exhibit an apparently rougher surface with nanoparticulate layers, and the diameter of each hybrid nanowire is expanded to 100–200 nm.

In good accordance with the above SEM results, transmission electron microscopy (TEM) image (inset in **Figure 3**a; top right) shows that the as-synthesized TO-MO hybrid nanowire array has an obvious core–shell structure. High-resolution TEM pictures are also displayed in Figure 3a,b, which confirm the presence of crystalline orthorhombic α-MoO_3 with characteristic plane of (101) (ca. 0.27 nm interspacing) and rutile TiO_2 with (101) plane (ca. 0.248 nm interspacing), respectively. The single-crystalline nature of particulate MoO_3 is further evidenced by the fast Fourier transformation (FFT) pattern in the inset of Figure 3a (bottom left), which clearly displays regular diffraction spots.

The composition of TO-MO hybrid electrode was directly studied by X-ray photoelectron spectroscopy (XPS). **Figure 4**a shows the XPS survey spectrum of α-MoO_3 and rutile TiO_2 with mainly the O 1s, Mo 3d, Mo 3p, Ti 2p, and Ti 2s peaks. Aside from the intense C 1s peak that is associated with the current collector substrate, only molybdenum, titanium and oxygen core levels can be observed. Figure 4b shows the symmetric peaks for the Mo 3d region (single doublet with binding energies of ca. 236.01 and 232.85 eV for the Mo $3d_{3/2}$ and Mo $3d_{5/2}$, respectively) indicating only the Mo^{6+} oxidation state. And the peaks with binding energies of ca. 464.7 and 458.7 eV are assigned to Ti $2p_{1/2}$ and Ti $2p_{3/2}$, respectively (Figure 4c), which confirm the presence of Ti^{4+} oxidation state. The crystallographic structure of TO-MO electrode was further analyzed by X-ray diffraction (XRD), as shown in Figure 4d. All the identified peaks can be indexed to the orthorhombic α-MoO_3 (JCPDS Card No. 05-0508) and rutile TiO_2 (JCPDS Card No. 21-1276). One broad and weak peak located at around 26° is the signal from the current collector.

2.2. Shell Optimization of the TO-MO Core–Shell Nanowire Array

Here, the deposition amount of the nano-MoO_3 shell, that is, the mass ratio of TiO_2 to MoO_3 for lithium storage should

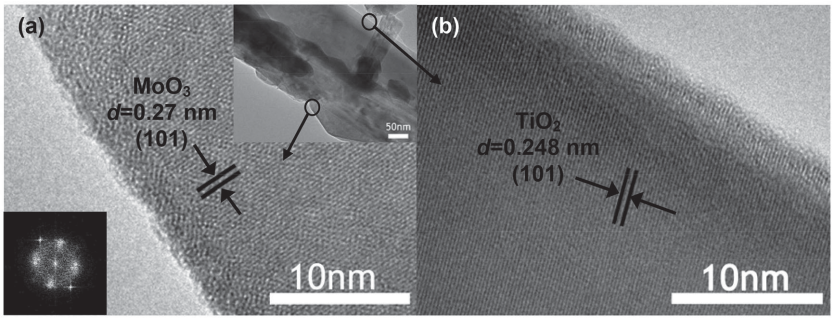

Figure 3. High-resolution TEM images of a) MoO_3 nanoparticulate shell and b) TiO_2 nanowire core (inset: low-magnification picture of the optimized TO-MO core–shell structure and FFT pattern of MoO_3).

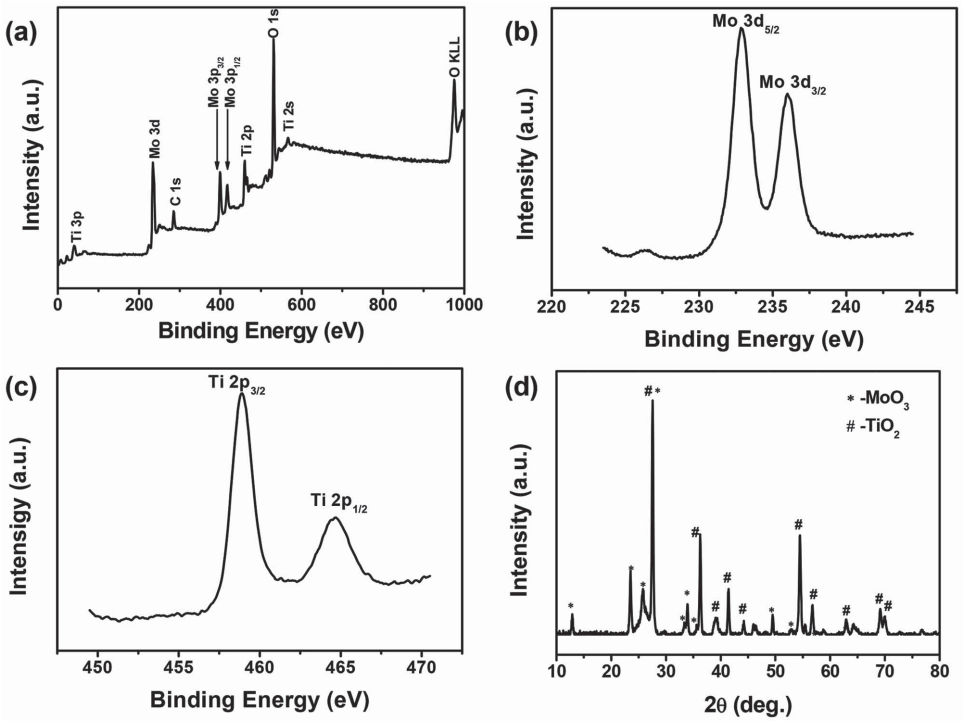

Figure 4. a) Typical XPS survey spectrum for the optimized TO-MO hybrid electrode. Binding energies of b) Mo 3d and c) Ti 2p components are shown. d) XRD pattern of the TO-MO hybrid electrode.

be considered. Generally, in order to increase the electrode capacity, the MoO_3 is expected to be deposited on unit area as much as possible, but the electrochemical performance, at the same time, is needed to remain stable; this makes the balanced hybridization of the core and shell highly necessary. From the SEM images of the TO-MO hybrid arrays with different MoO_3 mass loadings in **Figure 5**a–e, we found that the thickness of MoO_3 shell increases with the electrodeposition cycles increasing from 4 to 64 times, and the surface of TiO_2 nanowire array varies from partially covered to fully covered. Figure 5f illustrates the relationship between the MoO_3 mass loading and the cycle number of electrodeposition. It clearly indicates that the MoO_3 mass loading can be controllably tuned by adjusting electrodeposition times, and the mass of loaded nano-MoO_3 demonstrates nearly linear variation with the cycle number. With the areal mass of TiO_2 nanowire array of ca. 2.8 mg cm^{-2}, the approximate mass ratio of TiO_2 to 4, 8, 16, 32, 64 cycles deposited MoO_3 is 3:1, 5:2, 1.7:1, 1:1, and 1:1.6, respectively.

We then performed half-cell tests with working electrode of the pristine TiO_2 array or the TO-MO hybrid arrays with different MoO_3 mass loadings (counter electrode: Li foil). The

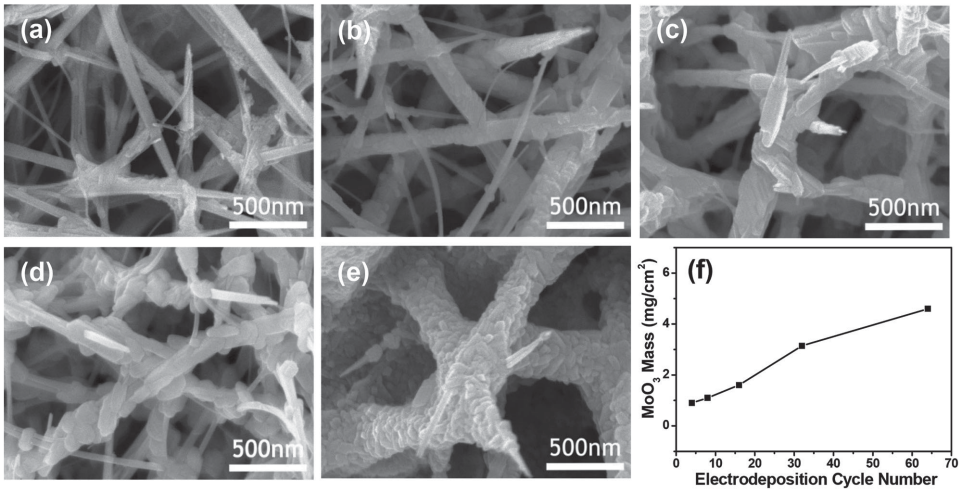

Figure 5. a–e) SEM images of different cycle number (4, 8, 16, 32, 64)-deposited TO-MO hybrid electrode. f) The plot for the relationship between the loading mass of MoO_3 and the electrodeposition cycle number.

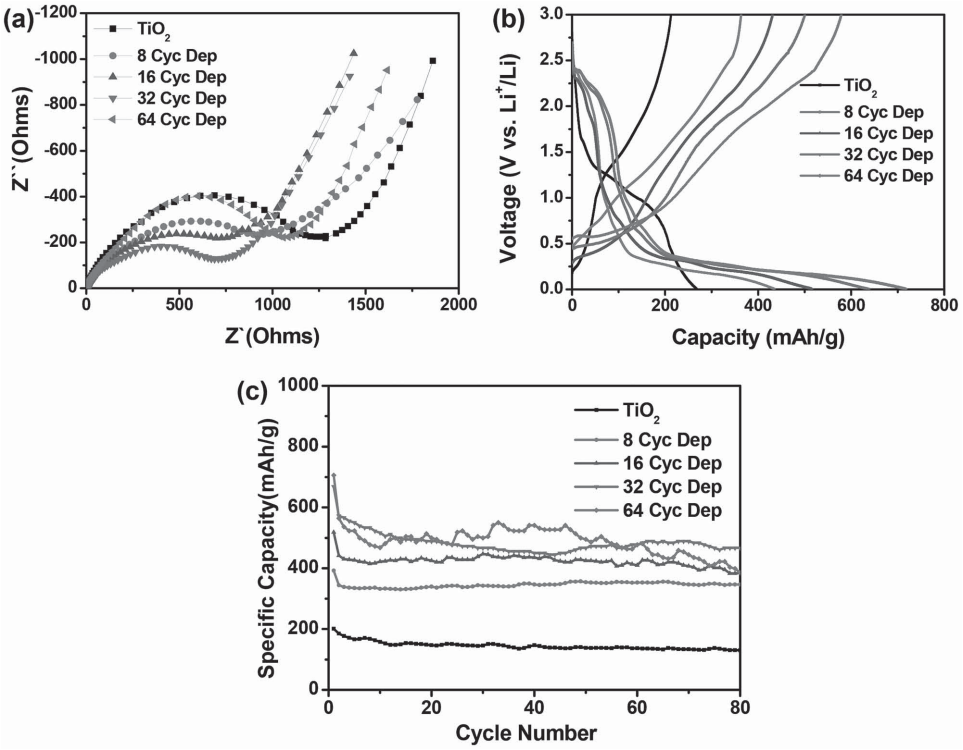

Figure 6. a) Nyquist plots of pristine TiO_2 nanowire array and different TO-MO samples. b) Charge–discharge voltage profiles and c) Cycling performances of different samples at 250 mA g^{-1}.

electrochemical impedance spectroscopy (EIS) was first used to provide electrochemical insights. The pristine TiO_2 electrode and different MoO_3 mass loaded TO-MO electrode's Nyquist plots taken in frequency range of 0.05 Hz–100 kHz at open circuit potential are shown in **Figure 6**a. All the EIS data are almost similar with a semicircle at the high frequency region and a spike at the low frequency region. The diameter of the semicircle is indicative of the charge-transfer resistance R_{ct}. Apparently, the pristine TiO_2 nanowire array has a higher R_{ct} than all of the TO-MO hybrid nanowire arrays, and from hybrid electrode with 8 cycles-deposited MoO_3 to that with 32 cycles-deposited MoO_3, the R_{ct} decreases gradually. This phenomenon confirms the presence of MoO_3 is beneficial to the electrical conductivity improvement and electrochemical activity. Nevertheless, the R_{ct} of the 64 cycles-deposited hybrid array is higher than those of other TO-MO samples. This should be due to the deposition of too thick nano-MoO_3 shell, in which numerous interconnected particles are assembled, producing many interfaces with high potential barriers that are harmful to electron transfer; furthermore, thick MoO_3 shell would also not be good for intimate electrolyte contact and thus deteriorates the interfacial charge transfer.

However, the optimal amount of MoO_3 shell should be determined by further considering the capacity and cycling stability. The first-cycle galvanostatic charge/discharge profiles of the pristine TiO_2 array and different TO-MO hybrid arrays with a potential range between 0.005 and 3.0 V (versus Li/Li^+) measured at 250 mA g^{-1} are shown in Figure 6b. As expected, the specific capacity of the hybrid array increases with prolonging the MoO_3 deposition cycle, and the 64 cycles-deposited TO-MO hybrid array shows the highest discharge capacity (ca. 718 mAh g^{-1}). However, for the 64 cycles-deposited sample, the capacity fades rapidly from the 50th cycle and approaches to only that of the 16 cycles-deposited TO-MO hybrid array after 80 cycles. By contrast, the 32 cycles-deposited TO-MO array shows the superior cycling stability to 64 cycles-deposited one and other TO-MO samples (Figure 6c). In combination with its relatively high capacity and Coulombic efficiency as well as the smallest R_{ct}, the 32 cycles-deposited TO-MO array (1:1 mass ratio) was regarded as the optimized electrode and has been used to carry out the following studies.

2.3. Electrochemical Performance of the Optimized TO-MO/Li Half Cell

The first two charge–discharge curves of the optimized (1:1) TO-MO nanowire array electrode at 250 mA g^{-1} are illustrated in **Figure 7**a. The differential capacity versus voltage plot of the first cycle is further provided in the inset of Figure 7a, which displays several characteristic peaks corresponding to the plateaus appeared in the 1st charge–discharge curve. For the hybrid electrode, detailed analysis of these differential peaks would give insightful information on the electrochemical mechanism.

The electrochemical *discharge* reaction mechanisms of Li with individual MoO_3 and TiO_2 have been well known and can be described as

$$MoO_3 + xLi^+ + xe^- \rightarrow Li_xMoO_3 \quad (1)$$

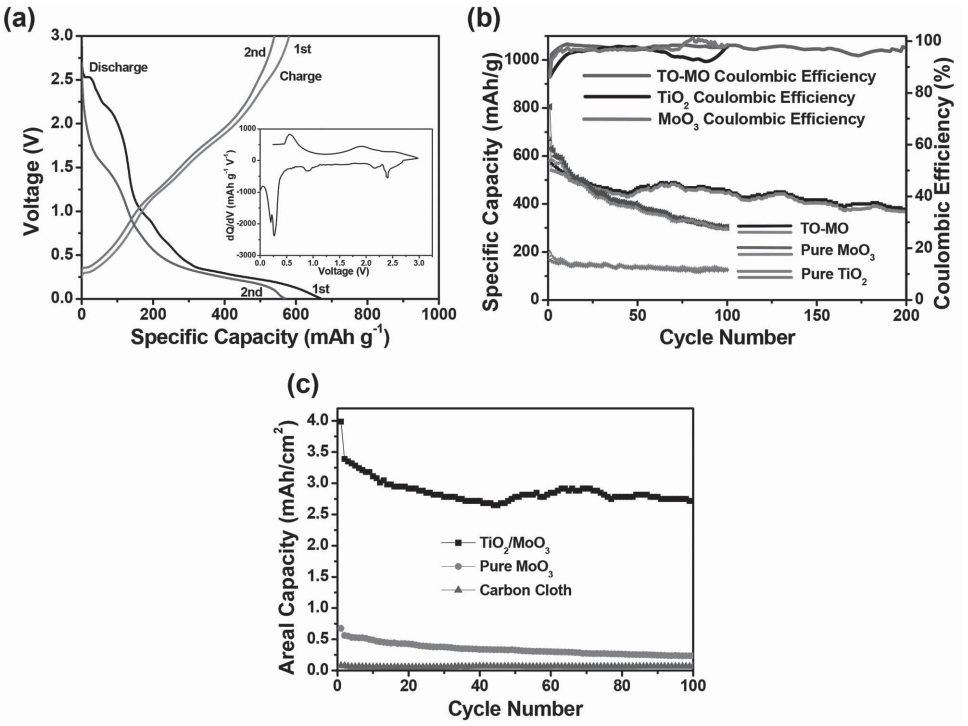

Figure 7. For the optimized TO-MO hybrid nanowire array electrode: a) the first and second charge–discharge curves at 250 mA g^{-1}. The inset is the corresponding differential capacity versus voltage plot for the first cycle. b) The cycling performance at 250 mA g^{-1}. Pristine MoO_3 nanofilm electrode and TiO_2 nanowire array electrode are also included for comparison. c) The areal capacity versus cycle number plots for TO-MO hybrid electrode, pristine MoO_3 nanofilm electrode and pure carbon cloth.

$$Li_xMoO_3 + (6-x)Li^+ + (6-x)e^- \rightarrow Mo + 3Li_2O \quad (2)$$

$$TiO_2 + xLi^+ + xe^- \rightarrow Li_xTiO_2 \quad (3)$$

Different from the pristine TiO_2 nanowire array electrode that only displays a relatively obvious plateau at ca. 1.1 V (Figure 6b), the optimized TO-MO electrode shows a small slope at ca. 2.4 V and a quite long plateau between 0.005–0.5 V as well as a sloping plateau from 0.75 to 1.25 V during the first discharge process. These observations correspond well with the differential charge–discharge curve. In the inset of Figure 7a, the small and broad peak centered at around 1.1 V is characteristic of the typical discharge process for hydrothermally grown rutile TiO_2[69] as Equation (3)[50,70]; this peak's intensity has been weakened due to the hybridization with the redox reactions occurring between Li^+ and MoO_3, evidenced by a steep slope profile (0.75–1.25 V) in the discharge curve. The peak at ca. 2.4 V is assigned to the Li^+ insertion into α-MoO_3 according to Equation (1),[28] and the peak around 0.27 V is related to the in-depth lithium uptake into Li_xMoO_3 by a unique conversion reaction to form Mo and Li_2O as Equation (2)[28,54] and the inevitable formation of a solid-electrolyte interface (SEI) layer. During the first charge process, the differential plot illustrates an obvious peak at ca. 0.7 V and a very broad peak ranging from 1.0 to 2.25 V, which can be ascribed to the reversible reaction of Equation (2) (multiphase process) with the superposition effect of the Li^+ deintercalation from Li_xTiO_2. A detectable but very weak and broad peak at ca. 2.5 V should be due to the desertion of Li^+ from crystalline Li_xMoO_3 (reversible reaction of Equation (1), but this reaction is not obvious since the discharge conversion reaction almost completely destroys the crystalline structure of MoO_3. This is also confirmed by the absence of the discharge plateau at ca. 2.4 V for the second cycle and can account for the capacity loss observed after the first cycle.

Figure 7b presents the cycling performance of optimized TO-MO nanowire array electrode up to 200 cycles at a current density of 250 mA g^{-1}. The data for pristine TiO_2 nanowire array and MoO_3 nanofilm synthesized under the same electrodeposition condition but without TiO_2 array are also included for comparison. For pure TiO_2, the first discharge capacity is slightly larger than 200 mAh g^{-1} and 74.7% can be retained after 100 cycles, demonstrating good cycling stability; but the reversible capacity value is only ca. 150 mAh g^{-1}. And the MoO_3 nanofilm electrode shows a high initial capacity of 805 mAh g^{-1}, but the capacity only remains 32% of the initial value after 100 cycles. By contrast, the TO-MO nanowire array electrode can organically integrate the merits of TiO_2 and MoO_3, simultaneously achieving high capacity and long cycling stability. Its initial capacity is ca. 670 mAh g^{-1}, very close to the theoretical value of the hybrid electrode of 723.5 mAh g^{-1} (for mass ratio of 1:1, the hybrid's theoretical capacity = $Q_{TiO2\ theoretical}$*50% + $Q_{MoO3\ theoretical}$*50% = 336 mAh g^{-1}*50% + 1111 mAh g^{-1}*50%); after 200 times of cycling, the capacity is still a bit larger than that of the commercial graphite anode. The Coulombic efficiency of the hybrid electrode is also kept at ca. 95% after the 10th cycle.

It is important to find that the 3D TiO_2 nanowire array can help to enhance the loading mass of MoO_3, which in reverse contributes to most of the absolute capacity of the TO-MO

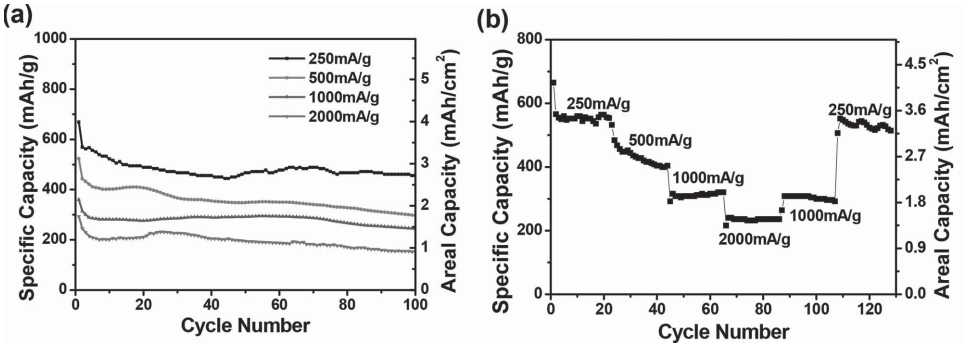

Figure 8. a) Cycling performance of the TO-MO hybrid electrode at different current rates and b) Cycling response at continuously variable current densities.

hybrid electrode. The deposited mass of pristine MoO_3 nanofilm directly on current collector is only ca. 0.9 mg cm^{-2}. From Figure 7c, it is clearly shown that for the first cycle the areal capacity of pure MoO_3 nanofilm (0.674 mAh cm^{-2}; note that the capacity contribution from pristine carbon cloth is negligible) is much lower than that of the TO-MO hybrid electrode (3.986 mAh cm^{-2}); and for the 100th cycle, the difference of the areal capacity between pure MoO_3 nanofilm and TO-MO hybrid electrode is extended to nearly 13 times (0.223 mAh cm^{-2} vs 2.842 mAh cm^{-2}). Therefore, the 3D TiO_2 array plays another crucial role in boosting the areal capacity of the MoO_3-based electrode, which is of significant importance for practical applications. To the best of our knowledge, the areal capacity of TO-MO electrode reported herein is not only comparable to that of the present commercial LIBs (ca. 3.7 mAh cm^{-2}), but also higher than many previous reports, such as silicon-based LIBs (ca. 3 mAh cm^{-2}),[59] nitrogen-doped carbon-sulfur nanocomposite lithium-sulfur batteries (ca. 3.3 mAh cm^{-2})[61] and folding paper-based LIBs (ca. 1.5 mAh cm^{-2}).[66]

Figure 8a shows the cycling performance of optimized TO-MO nanowire array electrode at different current densities, which reveals good cycling stability of the hybrid electrode at even high charge–discharge rates (the capacity fluctuation during cycling is possibly due to the fluctuation of environmental temperature). The specific capacity only decreases to 71%, 71.33%, 51.53%, and 58.73% after 100 cycles at the current density of 250, 500, 1000, and 2000 mA g^{-1}, respectively; and the capacity retains 53.38% and 45.86% with the current rate increasing from 250 to 500 and 1000 mA g^{-1}. This result is encouraging considering that our TO-MO electrode is entirely binder-free and carbon-free. The cycling stability during fast charge–discharge processes is better than other previous Mo-based LIB anodes.[28,35,54] The cycling response at continuously variable current was further evaluated and the results are displayed in Figure 8b. With the increase of the current density from 250 to 2000 mA g^{-1}, the specific capacity decreases accordingly, however, at each current density, the TO-MO hybrid electrode generally displays stable cycling behavior and when the current density turns back to the initial value, the capacity can almost recover. From the result, the TO-MO electrode is able to withstand a variety of different charge/discharge rates with good capacity recovery, which is highly desirable for high-power LIBs application.

Based on the above discussion, the optimized TO-MO nanowire array electrode not only has high capacity, but also shows long cycling stability and good rate performance. As expected (Figure 1), these should be attributed to the synergistic effect between TiO_2 nanowire array core (less volume change and structural destruction, providing stable support for large mass loading and distribution of MoO_3 and direct electron transport pathway as well as robust mechanical/electrical adhesion with current collector) and nano-MoO_3 shell (high capacity that remedies the inferior capacity of TiO_2, high electrical conductivity for electron transfer, etc.).

2.4. Evaluation of the Performance of LCO/TO-MO Full Cell

Next, in an effort to evaluate the practical application potential of our TO-MO hybrid electrode and to establish a more complete and practical energy storage device, a full-cell LIB was constructed with the optimized TO-MO nanowire array as the anode and the commercial $LiCoO_2$ (LCO) film (practical capacity is ca. 145 mAh g^{-1}) on Al foil as the cathode, as illustrated in **Figure 9**a. In order to rationally analyze the electrochemical performance, the mass ratio of the cathode and anode materials was chosen as 4:1 for charge balance and the following reported data for full cell are all based on the total mass of the LCO and TO-MO. Figure 9b displays the capacity versus current plots for both the TO-MO anode and LCO/TO-MO full cell. It is clearly indicated that the anode and the full cell store approximate charge at the same currents (3.315 mAh vs 3.123 mAh, 2.646 mAh vs 2.431 mAh, 1.836 mAh vs 1.688 mAh and 1.383 mAh vs 1.249 mAh at the current of ca. 1.5, 3, 6, and 9 mA, respectively), exhibiting comparable rate capability. This directly implies that the anode and cathode are highly matched.

The typical charge–discharge curves (1st to 3rd) of the LCO/TO-MO full cell at current density of 50 mA g_{total}^{-1} are presented in Figure 9c. The sloping potential plateaus at ca. 3.3 V (from 3.0 to 3.7 V) are observed for all the three charge–discharge processes, with the discharge capacity approaching 120 mAh g_{total}^{-1}. Figure 9d further shows the good cycling performance and high Coulombic efficiency of the full cell. The discharge capacity fades apparently only at the first several cycles but still can be cycled up to 100 times, while the Coulombic efficiency is maintained at almost 98% after the first cycle. Figure 9e illustrates cycling response of the LCO/TO-MO full cell at continuously variable current density. The specific capacity is as high as 120 mAh g_{total}^{-1} at the current density

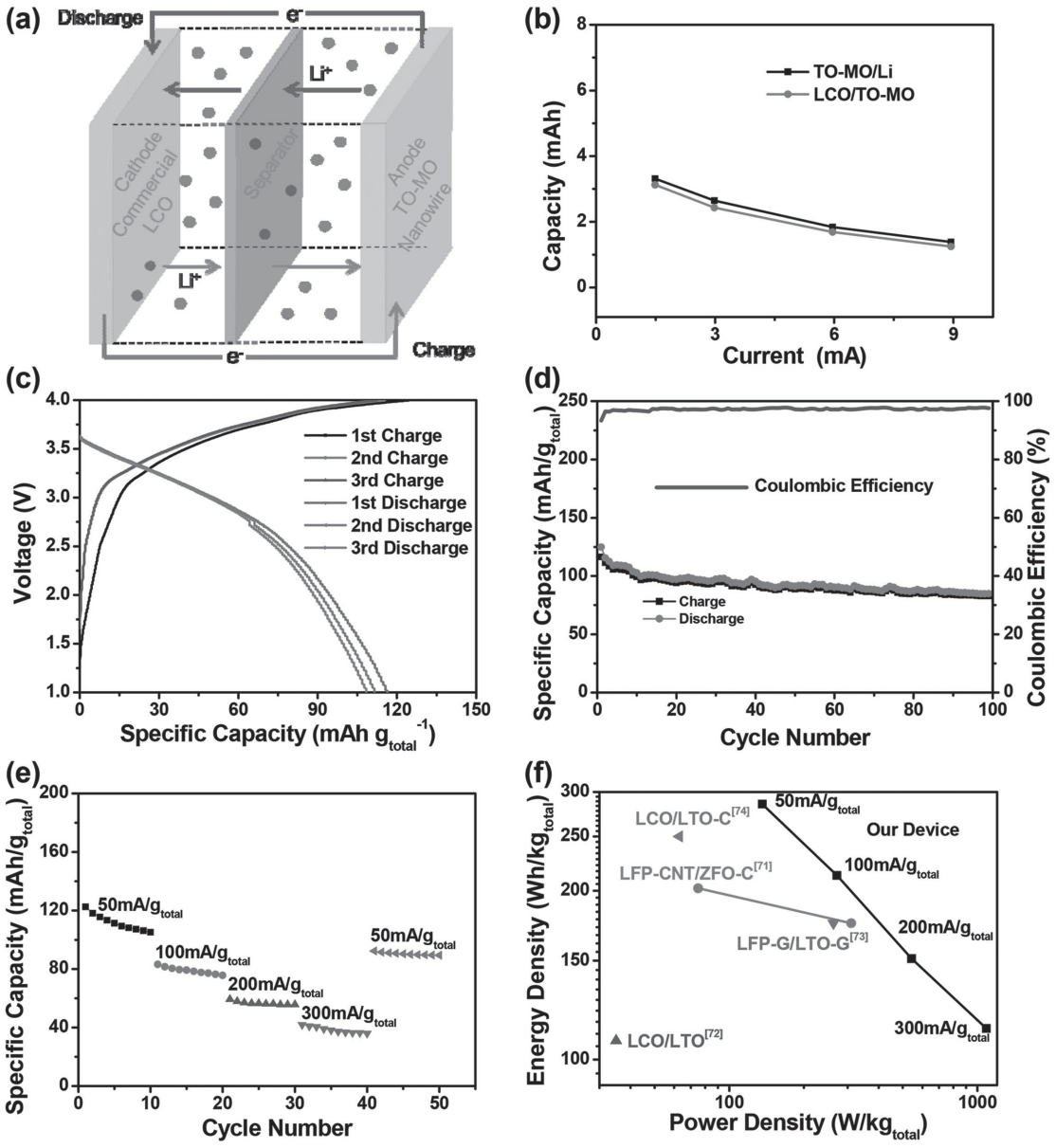

Figure 9. a) Schematic illustration of the LCO/TO-MO full cell. b) The stored charge of both the TO-MO/Li half cell and the full cell at different currents. c) The first three charge–discharge curves of the full cell. d) Cycling performance and Coulombic efficiency variation of the full cell at 50 mA g_{total}^{-1}. e) Cycling response at progressively increased current densities. f) Ragone plot of our full cell device. Data of previously reported full-cell LIB devices are also included for comparison.[71–74]

of 50 mA g_{total}^{-1}. As the current rate increases 6 times to 300 mA g_{total}^{-1}, the capacity of 40 mAh g_{total}^{-1} can still be delivered. Even suffering from a rapid variation of the current density, the full cell exhibits a relatively stable capacity at each current. In addition, when the current was turned back to 50 mA g_{total}^{-1}, most of the initial capacity can be recovered. The above results demonstrate again the advantages of the synergistic core–shell nanowire array architecture design of the anode.

For the future potential applications such as hybrid electric vehicles and multifunctional electronics, LIBs require not only high energy density but also high power density. Figure 9f shows Ragone plot of the LCO/TO-MO full cell, unveiling the relationship between energy and power densities. Some previous data in literature are also included for comparison. At the current density of 50 mA g_{total}^{-1}, the cell demonstrates the highest energy density of 285 Wh kg_{total}^{-1} (at which the power density is still around 136 W kg_{total}^{-1}); even if the current rate increases up to 300 mA g_{total}^{-1}, the energy density remains 114 Wh kg_{total}^{-1} with the corresponding power energy as high as 1086 W kg_{total}^{-1}. Our maximum energy density is much higher than most of the recently reported LIB full cell devices of $LiFePO_4$-CNT/$ZnFe_2O_4$-C (202 Wh kg^{-1} at 75 W kg^{-1}),[71] $LiCoO_2$/$Li_4Ti_5O_{12}$ (108 Wh kg^{-1} at 35 W kg^{-1}),[72] $LiFePO_4$-graphene/$Li_4Ti_5O_{12}$-graphene (175 Wh kg^{-1} at 263 W kg^{-1})[73] and

$LiCoO_2/Li_4Ti_5O_{12}$-C (250 Wh kg^{-1} at 63 W kg^{-1}),[74] for which the data were also calculated based on the total mass of both cathode and anode materials. It is believed that the energy density could be further increased by coupling our core–shell array anode with alternative high-potential cathode materials.

3. Conclusions

In summary, a hybrid TO-MO core–shell nanowire array anode has been successfully designed and fabricated through a simple hydrothermal method followed by an electrodeposition process. The optimized 1:1 TO-MO electrode exhibits high gravimetric capacity, good rate performance and cycleability owing to the synergistic interaction between the TiO_2 core and MoO_3 shell. Furthermore, benefiting from the 3D architecture of TiO_2 nanoarray, the areal capacity has been increased more than 10 times as compared to the pristine MoO_3 nanofilm attained directly on current collector under the same electrodeposition condition; it is even comparable to that of classical commercial LIBs. A full-cell LIB device assembled using TO-MO hybrid array as the anode and commercial LCO film as the cathode further manifests excellent performance in terms of both high energy density and power density, which are highly required for future applications. The concept of developing a synergistic core–shell nanowire array electrode can be readily extended to other LIB electrode designs, especially in the case that the electrode materials are superior in capacity but inferior in cycling stability and rate performance.

4. Experimental Section

Synthesis of TiO_2 Nanowire Array: The TiO_2 nanowire array was synthesized by a facile hydrothermal method. First, the precursor solution was prepared by mixing 21.2 mL acetone and 21.2 mL HCl with 1.5 mL tetrabutyl titanate. The mixed solution was stirred at room temperature until becoming clear. Before transferring the above solution into a Teflon-lined autoclave, an already seeded carbon cloth current collector was introduced and placed against the inner wall. Then, the precursor solution-loaded autoclave was sealed, heated to 200 °C and kept at this temperature for 2 h. After the reaction, the TiO_2 nanowire array-covered carbon cloth was cleaned with ethyl alcohol, dried at 60 °C in an oven, and finally subjected to heat treatment at 450 °C for 1 h to enhance the crystallinity of TiO_2. The seeding process was as follows: the bare carbon cloth was placed into a ca. 2.2 vol% $TiCl_4$ alcohol solution for 12 h with subsequent annealing at 400 °C for 1 h.

Synthesis of TO-MO Core–Shell Nanowire Array: For the synthesis of TO-MO hybrid array, electrodeposition was performed on a CS310 electrochemical workstation with a three-electrode model using TiO_2 nanowire array on carbon cloth as the working electrode, a Pt foil as the counter electrode, and an Ag/AgCl as the reference electrode. With the electrodeposition bath of 0.05 M $(NH_4)_6Mo_7O_{24}$ aqueous solution, the experiment was performed via cyclic voltammetry within 0 to −0.7 V at a sweep rate of 20 mV s^{-1} for different cycles (4 to 64 cycles). After the electrodeposition, the product was then annealed in Ar at 450 °C for 1h to obtain crystalline MoO_3-coated TiO_2 nanowires.

Characterizations: The morphology of the products was characterized by using SEM (JSM-6700F, 10.0 kV), TEM (JEM-2010FFF, 200 kV), XRD (Bruker D-8 Avance, Cu Kα), and XPS (VG 250 spectrometer, Al Kα 1486.6 eV). The mass of electrode materials was measured on a BS 124S Balance (max: 120 g; d = 0.1 mg). The weight of pure TiO_2 nanowire array and 4, 8, 16, 32, 64 cycles-deposited TO-MO hybrid array was 2.8, 3.7, 3.9, 4.4, 5.94, and 7.4 mg cm^{-2}, respectively.

Electrochemical Testing: The electrochemical performance of the TO-MO hybrid array was tested using Swagelok-type half cell, in which the counter and reference electrodes are Li-metal circular foil (0.59 mm thick). The half cell was assembled in an argon filled glove box with polypropylene (PP) film as the separator and a 1 M solution of $LiPF_6$ in ethylene carbonate (EC) and diethyl carbonate (DEC) (1:1 by volume) as the electrolyte. For the full cell testing, the TO-MO hybrid array was used as the anode and the commercial LCO film on Al foil as the cathode. After soaking with $LiPF_6$ electrolyte and separation by PP film, the electrodes were sealed with the same way to the half cell. After 8 h aging, the performance of both half cell and full cell was carried out at room temperature by using a multichannel battery tester (Shenzhen Neware Technology Co., Ltd, China). EIS measurements were performed by applying an AC voltage with 5 mV amplitude in a frequency range from 0.05 Hz to 100 kHz by using a CS310 electrochemical workstation. The full cell's energy density and average power density are calculated based on the equations $E = \int V(Q)dQ$ and $P = \frac{E}{t}$, respectively, where $V(Q)$ is the discharge voltage at Q, dQ is the differential charge element and t is the discharge time.

Acknowledgements

This work was supported by grants from the National Natural Science Foundation of China (Grant Nos. 51102105 and 11104088), the Science Fund for Distinguished Young Scholars of Hubei Province (Grant No. 2013CFA023), the Youth Chenguang Project of Science and Technology of Wuhan City (Grant No. 2014070404010206), Self-determined Research Funds of CCNU from the Colleges' Basic Research and Operation of MOE (CCNU14A02001), the Self-determined Innovation Foundation of Huazhong University of Science and Technology (Grant No. 2013027) and the Research Start-Up Fund from Wuhan University of Technology.

Received: February 14, 2015
Revised: April 12, 2015
Published online: May 4, 2015

[1] M. Armand, J. M. Tarascon, *Nature* **2008**, *451*, 652.
[2] Y. Wang, G. Z. Cao, *Adv. Mater.* **2008**, *20*, 2251.
[3] L. S. Li, F. Meng, S. Jin, *Nano Lett.* **2012**, *12*, 6030.
[4] C. Zhou, Y. W. Zhang, Y. Y. Li, J. P. Liu, *Nano Lett.* **2013**, *13*, 2078.
[5] H. S. Zhou, *Energy Environ. Sci.* **2013**, *6*, 2256.
[6] M. S. Whittingham, *Chem. Rev.* **2004**, *104*, 4271.
[7] Kang, G. Ceder, *Nature* **2009**, *458*, 190.
[8] a) H. Xia, C. Y. Hong, B. Li, B. Zhao, Z. X. Lin, M. B. Zheng, S. V. Savilov, S. M. Aldoshin, *Adv. Funct. Mater.* **2015**, *25*, 627; b) B. Liu, J. Zhang, X. F. Wang, G. Chen, D. Chen, C. W. Zhou, G. Z. Shen, *Nano Lett.* **2012**, *12*, 3005; c) Z. Chen, Y. C. Qin, D. Weng, Q. F. Xiao, Y. T. Peng, X. L. Wang, H. X. Li, F. Wei, Y. F. Lu, *Adv. Funct. Mater.* **2009**, *19*, 3420.
[9] a) B. Scrosati, *Nature* **1995**, *373*, 557; b) G. X. Wang, H. Liu, J. Liu, S. Z. Qiao, G. Q. Lu, P. Munroe, H. Ahn, *Adv. Mater.* **2010**, *22*, 4944; c) J. Z. Song, J. H. Li, J. Y. Xu, H. B. Zeng, *Nano Lett.* **2014**, *14*, 6298.
[10] a) C. K. Chan, H. Peng, G. Liu, K. McIlwrath, X. F. Zhang, R. A. Huggins, Y. Cui, *Nat. Nanotechnol.* **2008**, *3*, 31; b) L. F. Shen, E. Uchaker, X. G. Zhang, G. Z. Cao, *Adv. Mater.* **2012**, *24*, 6502; c) C. L. Yan, W. Xi, W. P. Si, J. W. Deng, O. G. Schmidt, *Adv. Mater.* **2013**, *25*, 539; d) M. S. Balogun, M. H. Yu, Y. C. Huang, C. Li, P. P. Fang, Y. Liu, X. H. Lu, Y. X. Tong, *Nano Energy* **2015**, *11*, 348.
[11] a) Y. L. Liu, Y. H. Xu, X. G. Han, C. Pellegrinelli, Y. J. Zhu, H. L. Zhu, J. Y. Wan, A. C. Chung, O. Vaaland, C. S. Wang, L. B. Hu, *Nano Lett.* **2012**, *12*, 5664; b) Y. G. Li, B. Tan, Y. Y. Wu, *Nano Lett.* **2008**, *8*, 265; c) X. H. Lu, G. M. Wang, T. Zhai, M. H. Yu, S. L. Xie, Y. C. Ling, C. L. Liang, Y. X. Tong, Y. Li, *Nano Lett.* **2012**, *12*, 5376.

[12] H. L. Pan, Y.-S. Hu, L. Q. Chen, *Energy Environ. Sci.* **2013**, *6*, 2338.
[13] X. H. Cao, Y. M. Shi, W. H. Shi, X. H. Rui, J. Kong, Q. Y. Yan, H. Zhang, *Small* **2013**, *9*, 1703.
[14] H. X. Ji, L. L. Zhang, M. T. Pettes, H. F. Li, S. S. Chen, L. Shi, R. Piner, R. S. Ruoff, *Nano Lett.* **2012**, *12*, 2446.
[15] H. G. Wang, D. L. Ma, X. L. Huang, Y. Huang, X. B. Zhang, *Sci. Rep.* **2012**, *2*, 701.
[16] K. T. Nam, D. W. Kim, P. J. Yoo, C. Y. Chiang, N. Meethong, P. T. Hammond, Y. M. Chiang, A. M. Belcher, *Science* **2006**, *312*, 885.
[17] B. A. Boukamp, G. C. Lesh, R. A. Huggins, *J. Electrochem. Soc.* **1981**, *128*, 725.
[18] M. Winter, J. O. Besenhard, M. E. Spahr, P. Novák, *Adv. Mater.* **1998**, *10*, 725.
[19] J. M. Tarascon, M. Armand, *Nature* **2001**, *414*, 359.
[20] X. J. Wang, R. Nesper, C. Villevieille, P. Novák, *Adv. Energy Mater.* **2013**, *3*, 606.
[21] M. F. Hassan, Z. P. Guo, Z. Chen, H. K. Liu, *J. Power Sources* **2010**, *195*, 2372.
[22] T. M. McEvoy, K. J. Stevenson, J. T. Hupp, *Langmuir* **2003**, *19*, 4316.
[23] M. S. Whittingham, *J. Electrochem. Soc.* **1976**, *123*, 315.
[24] J. O. Besenhard, J. Heydecke, E. Wudy, H. P. Fritz, W. Foag, *Solid State Ionics* **1983**, *8*, 61.
[25] S. Berthumeyrie, J. C. Badot, J. P. Pereira-Ramos, O. Dubrunfaut, S. Bach, Ph. Vermaut, *J. Phys. Chem. C* **2010**, *114*, 19803.
[26] J. Cabana, L. Monconduit, D. Larcher, M. R. Palacín, *Adv. Mater.* **2010**, *22*, E170.
[27] S. H. Lee, Y. H. Kim, R. Deshpande, P. A. Parilla, E. Whitney, D. T. Gillaspie, K. M. Jones, A. H. Mahan, S. B. Zhang, A. C. Dillon, *Adv. Mater.* **2008**, *20*, 3627.
[28] P. Meduri, E. Clark, J. H. Kim, E. Dayalan, G. U. Sumanasekera, M. K. Sunkara, *Nano Lett.* **2012**, *12*, 1784.
[29] Z. Q. Yuan, L. L. Si, D. H. Wei, L. Hu, Y. C. Zhu, X. N. Li, Y. T Qian, *J. Phys. Chem. C* **2014**, *118*, 5091.
[30] L. Q. Mai, B. Hu, W. Chen, Y. Y. Qi, C. S. Lao, R. S. Yang, Y. Dai, Z. L. Wang, *Adv. Mater.* **2007**, *19*, 3712.
[31] J. B. Jiang, J. L. Liu, S. J. Peng, D. Qian, D. M. Luo, Q. F. Wang, Z. W. Tian, Y. C. Liu, *J. Mater. Chem. A* **2013**, *1*, 2588.
[32] L. Zhou, L. C. Yang, P. Yuan, J. Zou, Y. P. Wu, C. Z. Yu, *J. Phys. Chem. C* **2010**, *114*, 21868.
[33] L. L. Cai, P. M. Rao, X. L. Zheng, *Nano Lett.* **2011**, *11*, 872.
[34] Z. Y. Wang, S. Madhavi, X. W. Lou, *J. Phys. Chem. C* **2012**, *116*, 12508.
[35] Y. X. Sun, J. Wang, B. Zhao, R. Cai, R. Ran, Z. P. Shao, *J. Mater. Chem. A* **2013**, *1*, 4736.
[36] J. S. Chen, Y. L. Cheah, S. Madhavi, X. W. Lou, *J. Phys. Chem. C* **2010**, *114*, 8675.
[37] J. Chang, M. H. Jin, F. Yao, T. H. Kim, V. T. Le, H. Y. Yue, F. Gunes, B. Li, A. Ghosh, S. Xie, Y. H. Lee, *Adv. Funct. Mater.* **2013**, *23*, 5074.
[38] A. M. Hashem, H. Groult, A. Mauge, K. Zaghib, C. M. Julien, *J. Power Sources* **2012**, *219*, 126.
[39] G. Y. Zhao, N. Q. Zhang, K. N. Sun, *J. Mater. Chem. A* **2013**, *1*, 221.
[40] X. F. Zhang, X. X. Song, S. Gao, Y. M. Xu, X. L. Cheng, H. Zhao, L. H. Huo, *J. Mater. Chem. A* **2013**, *1*, 6858.
[41] D. S. Guan, J. Y. Li, X. F. Gao, C. Yuan, *J. Power Sources* **2014**, *246*, 305.
[42] a) J. P. Liu, J. Jiang, C. W. Cheng, H. X. Li, J. X. Zhang, H. Gong, H. J. Fan, *Adv. Mater.* **2011**, *23*, 2076; b) J. Jiang, Y. Li, J. Liu, X. Huang, C. Yuan, X. W. Lou, *Adv. Mater.* **2012**, *24*, 5166.
[43] a) L. Yu, Z. Y. Wang, L. Zhang, H. B. Wu, X. W. Lou, *J. Mater. Chem. A* **2013**, *1*, 122; b) X. J. Hou, X. F. Wang, B. Liu, Q. F. Wang, Z. R. Wang, D. Chen, G. Z. Shen, *Chem. Electro. Chem.* **2014**, *1*, 108; c) J. Jiang, Y. Y. Li, J. P. Liu, X. T. Huang, *Nanoscale* **2011**, *3*, 45.
[44] a) W. M. Zhang, X. L. Wu, J. S. Hu, Y. G. Guo, L. J. Wan, *Adv. Funct. Mater.* **2008**, *18*, 3941; b) Y. Q. Wang, L. Gu, Y. G. Guo, H. Li, X. Q. He, S. Tsukimoto, Y. Ikuhara, L. J. Wan, *J. Am. Chem. Soc.* **2012**, *134*, 7874.
[45] a) S. H. Liu, Z. Y. Wang, C. Yu, H. B. Wu, G. Wang, Q. Dong, J. S. Qiu, X. W. Lou, *Adv. Mater.* **2013**, *25*, 3462; b) L. Q. Mai, F. Yang, Y. L. Zhao, X. Xu, L. Xu, Y. Z. Luo, *Nat. Commun.* **2011**, *2*, 381.
[46] a) J. Y. Liao, D. Higgins, G. Lui, V. Chabot, X. C. Xiao, Z. W. Chen, *Nano Lett.* **2013**, *13*, 5467; b) D. L. Chao, C. R. Zhu, X. H. Xia, J. L. Liu, X. Zhang, J. Wang, P. Liang, J. Y. Lin, H. Zhang, Z. X. Shen, H. J. Fan, *Nano Lett.* **2015**, *15*, 565.
[47] a) D. Z. Kong, J. S. Luo, Y. L. Wang, W. N. Ren, T. Yu, Y. S. Luo, Y. P. Yang, C. W. Cheng, *Adv. Funct. Mater.* **2014**, *24*, 3815; b) C. R. Zhu, X. H. Xia, J. L. Liu, Z. X. Fan, D. L. Chao, H. Zhang, H. J. Fan, *Nano Energy* **2014**, *4*, 105; c) X. Gu, L. Chen, Z. C. Ju, H. Y. Xu, J. Yang, Y. T. Qian, *Adv. Funct. Mater.* **2013**, *23*, 4049.
[48] G. J. Jeong, J. G. Kim, M. S. Park, M. Seo, S. M. Hwang, Y. U. Kim, Y. J. Kim, J. H. Kim, S. X. Dou, *ACS Nano* **2014**, *8*, 2977.
[49] H. Wang, D. Ma, X. Huang, Y. Huang, X. Zhang, *Sci. Rep.* **2012**, *2*, 701.
[50] Y. S. Luo, J. S. Luo, J. Jiang, W. W. Zhou, H. P. Yang, X. Y. Qi, H. Zhang, H. J. Fan, D. Y. W. Yu, C. M. Li, T. Yu, *Energy Environ. Sci.* **2012**, *5*, 6559.
[51] H. Xia, W. Xiong, C. K. Lim, Q. F. Yao, Y. D. Wang, J. P. Xie, *Nano Res.* **2014**, *7*, 1797.
[52] B. M. Sanchez, P. S. Grant, *Electrochim. Acta* **2013**, *98*, 294.
[53] Y. N. Ko, S. B. Park, K. Y. Jung, Y. C. Kang, *Nano Lett.* **2013**, *13*, 5462.
[54] Y. M. Sun, X. L. Hu, W. Luo, Y. H. Huang, *ACS Nano* **2011**, *5*, 7100.
[55] M. F. Hassana, Z. P. Guo, Z. Chen, H. K. Liu, *J. Power Sources* **2010**, *195*, 2372.
[56] F. Zhang, H. Q. Cao, D. M. Yue, J. X. Zhang, M. Z. Qu, *Inorg. Chem.* **2012**, *51*, 9544.
[57] J. X. Qiu, P. Zhang, M. Ling, S. Li, P. Liu, H. J. Zhao, S. Q. Zhang, *ACS Appl. Mater. Interfaces* **2012**, *4*, 3636.
[58] H. Han, T. Song, E. K. Lee, A. Devadoss, Y. Jeon, J. Ha, Y. C. Chung, Y. M. Choi, Y. G. Jung, U. Paik, *ACS Nano* **2012**, *6*, 8308.
[59] N. Liu, Z. D. Lu, J. Zhao, M. T. McDowell, H. W. Lee, W. Zhao, Y. Cui, *Nat. Nanotechnol.* **2014**, *9*, 187.
[60] Z. Yuan, H. J. Peng, J. Q. Huang, X. Y. Liu, D. W. Wang, X. B. Cheng, Q. Zhang, *Adv. Funct. Mater.* **2014**, *24*, 6105.
[61] J. X. Song, T. Xu, M. L. Gordin, P. Y. Zhu, D. P. Lv, Y. B. Jiang, Y. S. Chen, Y. H. Duan, D. H. Wang, *Adv. Funct. Mater.* **2014**, *24*, 1243.
[62] X. L. Dong, Z. Y. Guo, Y. F. Song, M. Y. Hou, J. Q. Wang, Y. G. Wang, Y. Y. Xia, *Adv. Funct. Mater.* **2013**, *4*, 1.
[63] X. H. Wang, Y. Fan, R. A. Susantyoko, Q. Z. Xiao, L. M. Sun, D. He, Q. Zhang, *Nano Energy* **2014**, *5*, 91.
[64] R. Yi, J. T. Zai, F. Dai, M. L. Gordin, D. H. Wang, *Nano Energy* **2014**, *6*, 211.
[65] Q. Z. Xiao, Y. Fan, X. H. Wang, R. A. Susantyokoa, Q. Zhang, *Energy Environ. Sci.* **2014**, *7*, 655.
[66] Q. Cheng, Z. M. Song, T. Ma, B. B. Smith, R. Tang, H. Y. Yu, H. Q. Jiang, C. K. Chan, *Nano Lett.* **2013**, *13*, 4969.
[67] J. X. Song, Z. X. Yu, T. Xu, S. R. Chen, H. Sohn, M. Regula, D. H. Wang, *J. Mater. Chem. A* **2014**, *2*, 8623.
[68] J. Q. Huang, H. J. Peng, X. Y. Liu, J. Q. Nie, X. B. Cheng, Q. Zhang, F. Wei, *J. Mater. Chem. A* **2014**, *2*, 10869.
[69] Z. Q. Sun, J. H. Kim, Y. Zhao, F. Bijarbooneh, V. Malgras, Y. Lee, Y. M. Kang, S. X. Dou, *J. Am. Chem. Soc.* **2009**, *131*, 9152.
[70] G. Sudant, E. Baudrin, D. Larcher, J. M. Tarascon, *J. Mater. Chem.* **2005**, *15*, 1263.
[71] A. Varzi, D. Bresser, J. V. Zamory, F. Müller, S. Passerini, *Adv. Energy Mater.* **2014**, *4*, 1400054.
[72] L. Hu, H. Wu, F. La Mantia, Y. Yang, Y. Cui, *ACS Nano* **2010**, *4*, 5843.
[73] N. Li, Z. Chen, W. Ren, F. Li, H. M. Cheng, *Proc. Natl. Acad. Sci. U. S. A.* **2012**, *109*, 17360.
[74] J. Liu, K. Song, P. A. V. Aken, J. Maier, Y. Yu, *Nano Lett.* **2014**, *14*, 2597.